



Cite this: *Phys. Chem. Chem. Phys.*,
2022, 24, 4174

The molecular origin of the electrostatic gating of single-molecule field-effect biosensors investigated by molecular dynamics simulations†

Sébastien Côté,^{ib}*^{ab} Delphine Bouilly^{ib}*^{ac} and Normand Mousseau*^a

Field-effect biosensors (bioFETs) offer a novel way to measure the kinetics of biomolecular events such as protein function and DNA hybridization at the single-molecule level on a wide range of time scales. These devices generate an electrical current whose fluctuations are correlated to the kinetics of the biomolecule under study. BioFETs are indeed highly sensitive to changes in the electrostatic potential (ESP) generated by the biomolecule. Here, using all-atom solvent explicit molecular dynamics simulations, we further investigate the molecular origin of the variation of this ESP for two prototypical cases of proteins or nucleic acids attached to a carbon nanotube bioFET: the function of the lysozyme protein and the hybridization of a 10-nt DNA sequence, as previously done experimentally. Our results show that the ESP changes significantly on the surface of the carbon nanotube as the state of these two biomolecules changes. More precisely, the ESP distributions calculated for these molecular states explain well the magnitude of the conductance fluctuations measured experimentally. The dependence of the ESP with salt concentration is found to agree with the reduced conductance fluctuations observed experimentally for the lysozyme, but to differ for the case of DNA, suggesting that other mechanisms might be at play in this case. Furthermore, we show that the carbon nanotube does not impact significantly the structural stability of the lysozyme, corroborating that the kinetic rates measured using bioFETs are similar to those measured by other techniques. For DNA, we find that the structural ensemble of the single-stranded DNA is significantly impacted by the presence of the nanotube, which, combined with the ESP analysis, suggests a stronger DNA–device interplay. Overall, our simulations strengthen the comprehension of the inner working of field-effect biosensors used for single-molecule kinetics measurements on proteins and nucleic acids.

Received 8th October 2021,
Accepted 11th December 2021

DOI: 10.1039/d1cp04626h

rsc.li/pccp

Introduction

Field-effect transistor biosensors (bioFETs) are electronic circuits designed to monitor a wide variety of biomolecular processes *via* variations in their electric current.^{1–7} They are used, for instance, to detect the concentration of specific agents such as hazardous molecules,⁸ biomarkers,⁹ DNA sequences,¹⁰ pH,¹¹ ion concentration¹² and viruses.¹³ They can also be ultraminiaturized to measure the single-molecule kinetics of protein function¹⁴ as well as DNA hybridization¹⁵ and folding.¹⁶

The main component of a single-molecule bioFET is a low-dimensional field-effect transistor, often made of a carbon nanotube or nanowire joining two electrodes.^{17,18} These ultra-confined electrical channels are specifically chosen because their electronic properties are strongly dependent on the local electric field. As such, their conductance is very sensitive to the structure of biomolecules when they are localized near them. For single-molecule bioFETs using a carbon nanotube, the biomolecule under investigation is localized on the surface of the nanotube through the formation of a covalent bond or π -interactions. Therefore, as the biomolecule folds or performs its function, the conductance of the bioFET changes, likely due to changes in the electrostatic potential (ESP) at the surface of the carbon nanotube. By analyzing the kinetics of the conductance measured by the device as a function of time, the kinetics of the biomolecule can be unveiled, as supported by several experimental studies based on such devices.^{14–16,19–25}

In a key study focusing on a protein, Choi *et al.* investigated the T4 lysozyme enzyme kinetics as it cleaves a peptidoglycan,

^a Département de Physique, Faculté des Arts et des Sciences, Université de Montréal, Montréal, Canada. E-mail: sebastien.cote.4@umontreal.ca, normand.mousseau@umontreal.ca

^b Département de Physique, Cégep de Saint-Jérôme, Saint-Jérôme, Canada

^c Institut de recherche en immunologie et oncologie (IRIC), Université de Montréal, Montréal, Canada. E-mail: bouilly@umontreal.ca

† Electronic supplementary information (ESI) available: Details on the parameterization of the linkers as well as supplementary figures and tables for the analysis. See DOI: 10.1039/d1cp04626h

such as found in bacterial cell walls, using a carbon nanotube bioFET.¹⁴ They showed that the conductance of the nanotube exhibits two-level fluctuations as the lysozyme is performing its function. Moreover, the measured kinetic rates from the conductance are comparable to those measured for lysozyme using other techniques such as single-molecule fluorescence resonance energy transfer (FRET), while allowing measurements on longer time scales. In a following study, they investigated in more details the mechanisms responsible for the two-level fluctuations of the nanotube's conductance.²² They observed that these fluctuations depend on the electrostatic screening incurred by the lysozyme due to the electrolyte's ionic strength, suggesting that the gating mechanisms of the biomolecule on the nanotube are mainly electrostatic in nature. To strengthen this observation, they performed mutagenesis of the lysozyme showing that the conductance fluctuations are affected by two charged amino acids – Lys-83 and Arg-119 – that are located near the attachment site on the nanotube.

For nucleic acids, Sorgenfrei *et al.* investigated the hybridization kinetics of 10 nt DNA sequences using a carbon nanotube bioFET.¹⁵ They also measured two-level conductance fluctuations with kinetic rates comparable to those obtained using FRET. In a following study, they characterized in more details the conductance fluctuations of the nanotube during DNA hybridization.¹⁹ They observed that the magnitude of the two-level conductance fluctuations depends on the ionic concentration of the solution, again suggesting that the gating mechanisms are mainly electrostatic in nature. Moreover, they showed that the nucleic acids nearest to the attachment site on the nanotube are most responsible for the fluctuations in the conductance because they are less electrostatically screened by the electrolyte solution.

Taken together, these experimental results strongly suggest that the conductance kinetics of the carbon nanotube bioFET depends directly on the electrostatic potential generated by the biomolecule as it performs its function or as it folds. Following studies based on similar constructs also support this view: on the interaction between the immunoglobulin E antibody and an aptamer-modified carbon nanotube,²⁶ on DNA hybridization^{20,21} and folding¹⁶ as well as on the function of the several enzymes such as the Klenow fragment of DNA polymerase I,^{23,27} the β -lactamase,²⁸ the Histone deacetylase 8,²⁹ the protein kinase A,²⁴ and the lysozyme.^{25,30,31} Similar observations were also made using a silicon nanowire-based field-effect transistor (SiNW-FET).^{18,32}

To gain a deeper understanding of the inner working of single-walled carbon nanotube FETs (SWCNT-bioFETs), *ab initio* studies investigated the binding energies of nucleic bases and amino acids as well as their impact on the electronic structure of SWCNT and graphene.^{33–35} On single base–SWCNT interactions, *ab initio* calculations indicate that bases are forming π – π interactions with SWCNT and that their interaction energies depend on the base type.³⁶ External electric-field has also been shown to influence the interaction energy and the density of states, but not the geometry of the base.³⁷ A more recent work also indicates that adenosine monophosphate (AMP) changes the band-gap of

semi-conducting SWCNT, but not that of metallic SWCNT, mainly due to the negatively charged phosphate group.³⁸ On single amino acid–SWCNT interaction, *ab initio* calculations also indicate that aromatic amino acids (Phe, His, Tyr and Trp) form π – π interactions with SWCNT and affect the electronic spectra.^{39,40} Hybrid QM/MM calculations were also performed to explicitly consider water molecules revealing a strong adsorption of the bases on SWCNT (stronger than in vacuum), a small charge transfer from SWCNT to the base and an electrostatic potential dominated by the phosphate group.^{41,42} Yet, the bridge between the single amino acid/nucleotide and biomolecules is not complete because *ab initio* calculations are limited to small spatial or time scales. A more thorough sampling, at the molecular level on longer time scales, of the electrostatic potential generated by the biomolecules on the surface of the nanotube could help to bridge this gap.

Another fundamental aspect of the inner working of SWCNT-bioFETs is the interactions taking place between the biomolecules under investigation and the carbon nanotube at the core of the device. SWCNT–DNA interactions are at the focus of many studies^{43,44} as single-stranded DNA (ssDNA) can be used to disperse and separate SWCNT based on their chirality.^{45,46} For instance, temperature assays were used to quantify the association and dissociation of ssDNA to SWCNT and they indicated that the stability of the interactions depends on the DNA sequence.⁴⁷ Furthermore, analysis of optical absorption spectra indicates that specific ssDNA sequences bind to specific SWCNT chirality.⁴⁸ A more recent study showed, using single-molecule force spectroscopy, that ssDNA can wrap around the nanotube and that the compactness of this fold depends on the ionic concentration of the solution because it affects the formation of base–base H-bonds.⁴⁹

Many simulations were also designed to explore the structural ensemble of biomolecules on SWCNT and on graphene.³³ Molecular dynamics (MD) simulations show that single-stranded DNAs (ssDNA) bind quickly to the surface of the SWCNT and undergo structural changes, while double-stranded DNAs stay stable.⁵⁰ Longer MD and replica-exchange MD (REMD) revealed that the (GT)₇ oligonucleotide adopts a wide variety of SWCNT-adsorbed configurations – some compact or extended, others wrapped around the surface – that are stabilized by DNA–SWCNT π – π and DNA–DNA H-bonds interactions.^{51,52} Similar observations were made from another REMD simulation on the decamer oligonucleotides of T only, G only or alternating TG.⁵³ Again using REMD, it was also shown that these structural ensembles are sensitive to the diameter of the nanotube.⁵⁴ The interaction of 1 to 4 ssDNA strands on SWCNT has also been investigated using REMD revealing that these assemblies are stabilized by π – π stacking between the DNA bases and the SWCNT, but also by a number of non-Watson Crick H-bonds.⁵⁵ Recently, the structural ensemble of 36 sequences of 10, 11 and 12 nt ssDNA on SWCNT has been investigated using REMD simulations showing that these adopt ring and helix-like configurations, the precise balance depending on the sequence.⁵⁶ Protein–SWCNT interactions have also been investigated, revealing that these interactions can be sufficient to perturb their functional regions.^{57,58} Yet, a thorough sampling at the

molecular level of the interactions between SWCNT–biomolecules (proteins, ssDNA and dsDNA) in the context of the SWCNT–bioFET device remains to be done because the biomolecule is covalently grafted or non covalently anchored to the SWCNT and because few simulations were performed on the interactions of large protein or dsDNA with SWCNT.

In this study, we use all-atom solvent explicit molecular dynamics simulations to further characterize at the molecular level two systems previously characterized experimentally using the carbon nanotube bioFET for single-molecule kinetics measurements: (1) the function of the lysozyme enzyme^{14,22} and (2) the hybridization of a 10 nt DNA duplex.^{15,19} More specifically, we investigate the fluctuations of the electrostatic potential on the surface of the carbon nanotube as the state of these biomolecules changes, and we relate those to the conductance fluctuations measured experimentally. Furthermore, we investigate the interactions between the carbon nanotube and these biomolecules as well as their impact on the structural stability of these biomolecules.

Methodology

We perform molecular dynamics simulations to characterize the evolution of two systems – the function of the lysozyme enzyme and the hybridization of a DNA strand – in solution and in the presence of the carbon nanotube. These two systems were chosen because the carbon nanotube field-effect biosensor (bioFET) has already been characterized experimentally for these, allowing a more direct comparison of our results with experiment.^{19,22} The initial states of our simulations are shown in Fig. 1 as well as in Fig. S1 and S2 (ESI[†]), and they are described below in details.

General setup

Our molecular dynamics simulations are done with the software GROMACS-2019⁶⁰ in the *NVT* ensemble at 300 K using the Bussi–Donadio–Parrinello thermostat.⁶¹ Covalent bonds involving a hydrogen atom are constrained using the algorithm LINCS⁶² and the geometry of water molecules is constrained using the algorithm SETTLE.⁶³ The cutoff for short range Lennard-Jones and electrostatics interactions is 1 nm. Long range electrostatics interactions are computed using the smooth particle-mesh Ewald method.⁶⁴ A dispersion correction for long range Lennard-Jones interactions is applied to the pressure (during equilibration) and to the total energy. The integration time step is 2 fs. Each system is prepared as follow: (1) it is solvated with TIP3P water molecules⁶⁵ as well as Joung–Cheatham Na/Cl ions⁶⁶ to achieve neutrality and the desired ionic concentration (see below for each system), (2) it is minimized using sequentially the steepest descent and conjugate gradient algorithms, (3) the temperature is then equilibrated at 300 K for 1 ns while restraining the non-hydrogen atoms of the protein/ligand or DNA strand and (4) finally the pressure is equilibrated at 1 atm for 1 ns while restraining the non-hydrogen atoms of the protein/ligand or DNA strand.

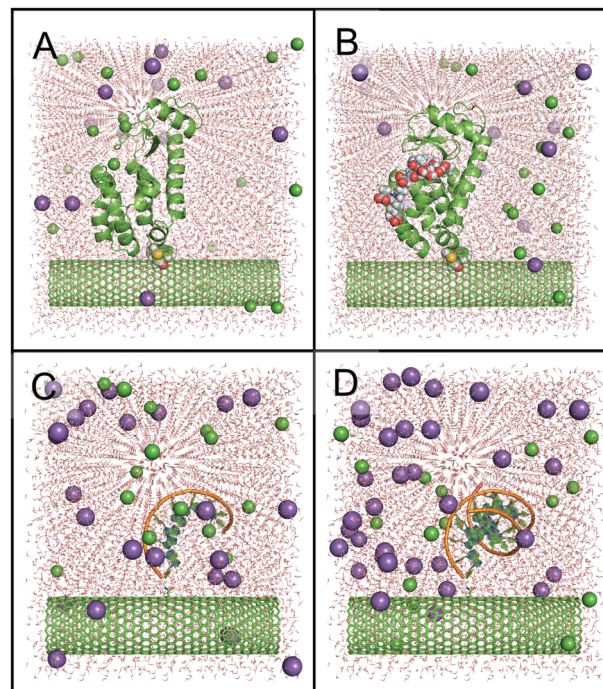


Fig. 1 Initial systems. (A) Lysozyme without the ligand (PDB: 1QTV) and (B) with the peptidoglycan ligand shown using spheres and carbon atoms in teal (PBD: 148L). The pyrene-maleimide anchor to the nanotube is covalently linked to S90C of the lysozyme and is shown using spheres. (C) The single-stranded 5'-GTGAGTTGTT-3' DNA sequence and (D) the B-DNA double-stranded sequence covalently linked to the carbon nanotube. The sodium and chloride ions are respectively shown as purple and green spheres. The images were produced with PyMOL.⁵⁹

Carbon nanotube

In the experimental setup, the nanotubes produced have a diameter between 1.1 and 1.6 nm^{14,22} or of at most 2.0 nm^{15,19} as measured by atomic force microscopy (AFM). Their chirality, for their part, have not been determined in these experiments and it is likely to be heterogeneous. For our simulations, a type (18, 0)-zigzag nanotube is used because it has a diameter (1.4 nm) that is similar to what has been measured experimentally and because it has been previously used to estimate the electrostatic potential generated by rigid, extended and upright single-stranded and double-stranded DNAs on the surface of a nanotube.¹⁹

The nanotube is considered to be infinite in our simulations because its length is on the order of a few μm in the experimental setup, which is much greater than the size of the attached biomolecule.^{14,15,19,22} We chose to align the nanotube axis with the *z*-axis such that it occupies the whole length of the simulation box. The length of the nanotube has been chosen to avoid intramolecular interactions of the lysozyme (nanotube has 17 unit cells: 7.14 nm in length) and the DNA segment (nanotube has 14 unit cells: 5.88 nm in length) with their periodic images. *NPT* equilibration for the systems with a carbon nanotube used anisotropic pressure coupling to maintain the size of the box fixed in *z*.

Finally, the atoms of the carbon nanotube are considered as uncharged sp^2 carbon with Lennard-Jones parameters $\sigma = 0.339967$ nm and $\varepsilon = 0.359824$ kJ mol⁻¹ (type CA in AMBER).

Lysozyme

The lysozyme systems are prepared in line with the bioFET characterized experimentally by Choi *et al.*²² We simulate the T4 lysozyme attached to a carbon nanotube in a 50 mM NaCl solution (Fig. 1A and B). The T4 lysozyme enzyme is a bacteriophage that binds to and cleaves peptidoglycans on bacterial cell walls. Its structures without (PDB: 1QTV) and with (PDB: 148L) the peptidoglycan ligand were determined using X-ray crystallography.^{67,68} These structures were slightly modified using PyMOL⁵⁹: (1) the E26T change is done to recover the native sequence and (2) N163 and L164 are added at the end of 148L such that it has the same sequence as 1QTV. The interactions of the protein are modeled using AMBER14sb because it improves the structural ensemble of both side-chains and main-chains compared to experiment.⁶⁹ The ligand in the bound state is parameterized with GAFF using ACPYPE,^{70,71} with partial charges determined using AM1-BCC calculations.⁷²

In the experimental construct of the lysozyme attached to the bioFET, the lysozyme is covalently conjugated to a pyrene-maleimide molecule that adheres on the surface of the nanotube through π - π stacking.²² To do so, the S90C mutation is performed on the lysozyme to allow the formation of a covalent bond with the thiol reactive pyrene-maleimide compound. For our simulations, we prepared our systems such that the aromatic rings of the pyrene are already stacked on the surface of the nanotube and we then covalently linked it to S90C of the lysozyme. We restrain the position of the pyrene's carbon atoms during the simulations. The parameters of the pyrene-maleimide compound covalently attached to the cysteine are determined with GAFF using ACPYPE.^{70,71} The partial charges were determined using *ab initio* HF calculations following the protocol used for the AMBER force field for proteins⁷³ (see ESI† for more details).

DNA

The DNA systems are prepared in line with the biosensor characterized experimentally by Sorgenfrei *et al.*¹⁹ We simulate the 5'-GTGAGTTGTT-3' DNA strand covalently linked to a carbon nanotube in a 100 mM NaCl solution (Fig. 1C and D). We prepared the single DNA strand and the hybridized B-DNA sequence using PyMOL.⁵⁹ The interactions of the nucleic acids are modeled using AMBER-OL15 because it improves the structural ensemble of the dihedral angles χ , ϵ , ζ and β for A-DNA, B-DNA, Z-DNA and non-canonical folds compared to experiment.⁷⁴

In the experimental construct of the DNA strand attached to the bioFET, the DNA 5'-end has an amine group that forms a covalent bond with a carboxylic acid defect on the surface of the carbon nanotube.¹⁹ For our simulations, we covalently linked the carbon nanotube with the C5' of the DNA 5'-end with an amide group, which is the end product of the reaction in the experiment. The linker between the nanotube and the DNA strand is parameterized with GAFF using ACPYPE.^{70,71} The partial charges were determined using *ab initio* HF calculations following the protocol used for the AMBER force field for nucleic acids⁷³ (see ESI† for more details).

Analysis

The extraction of relevant data from the molecular dynamics trajectories is done using GROMACS tools. Data analysis and graphics are done using in-house tools in Python. The secondary structure of the protein is determined using DSSP.^{75,76} A residue-residue contact is considered when the distance is less than 0.35 nm between any two atoms for residues spaced by at least one residue in the sequence. A hydrogen bond is considered when the donor-acceptor distance is less than 0.35 nm and the hydrogen-donor-acceptor angle is less than 30°. All molecular images are prepared with PyMOL.⁵⁹

The electrostatic potential generated by the protein/ligand or the DNA strands on the surface of the carbon nanotube is computed using APBS (version 1.3).⁷⁷ The non-linear Poisson-Boltzmann equation is solved on a discretized box with a resolution of 0.5 Å. The dimensionless dielectric constant is set to 2.0 (solute/internal) and 80.0 (solvent/external). To determine the accessible surface of the solute, the water molecule probe radius is set to 0.14 nm and the ion radius is set to 0.20 nm. The boundary potentials are calculated by the dipole approximation using the Debye-Hückel potential. The electrostatic potential on the surface of the carbon nanotube is computed for the following NaCl salt concentrations: 0.01 M, 0.02 M, 0.05 M, 0.10 M, 0.20 M and 0.30 M. In all systems, the presence of the nanotube is taken into account. The box dimension is 144.5 × 144.5 × 144.5 Å³ for the lysozyme systems and 112.5 × 112.5 × 112.5 Å³ for the DNA systems, resulting in a dimension scaling of more than 2.0 with respect to the dimensions of the biomolecules. The box is centred on the biomolecule in *x* and *y* and it is centred on the nanotube in *z*. The nanotube's length is extended to 107.1 Å (*vs.* 71.4 Å in the MD) for the lysozyme systems and to 98.0 Å (*vs.* 58.8 Å in the MD) for the DNA systems in order to take into account the crossing that sometimes occurs through the periodic boundaries during the MD. The partial charges of the pyrene-maleimide linker of the lysozyme and the partial charges of the covalent linker of the DNA are set to zero for these computations in order to focus on the longer-range electrostatic potential generated by the biomolecules.

The interval of convergence chosen for the analysis of each simulation is discussed in the ESI.†

Results and analysis

We investigate the following three main points for both the lysozyme and the DNA systems: (1) the structural stability of the biomolecules in the presence of the carbon nanotube, (2) the interactions between the biomolecules and the nanotube and (3) the electrostatic potential generated by the biomolecules on the surface of the nanotube. Two states are simulated for the lysozyme – with and without the peptidoglycan ligand, respectively referred to lysozyme and lysozyme-ligand in the following – and for the 5'-GTGAGTTGTT-3' DNA sequence – single-stranded and double-stranded, respectively referred to ssDNA and dsDNA in the following. Each of these four systems

is simulated in solution (two 1 μ s simulations each) and then attached to a carbon nanotube (five 1 μ s simulations each).

Structural stability of the biomolecules

Lysozyme. We first analyze the impact of the carbon nanotube on the structural stability of the lysozyme and lysozyme-ligand systems (Table 1). To do so, we compare their respective structural ensemble in solution to those in the presence of the carbon nanotube in terms of root mean square deviation (RMSD), secondary structure and percentage of contact similarity against the experimental crystal structures.

In solution, the structural ensembles of the lysozyme and lysozyme-ligand systems remain close to their respective experimental crystal structure, with an average RMSD of 0.98 Å and 1.43 Å, respectively (S-Avg lines in Table 1). Similarly, their secondary structures – comparable α -helix, β -sheet and coil probabilities, albeit a slightly smaller α -helix probability compared to the crystal structure – and their contact similarity – around 92% – indicate that these two lysozyme states are stable in solution.

Linking each molecular systems to a carbon nanotube has little impact on their structure. Indeed, comparing the S-Avg lines to the C-Avg lines, which show the structural properties averaged over the independent simulations respectively in solution and in the presence of the carbon nanotube, we see

Table 1 Structural stability of lysozyme. The MD trajectories of the lysozyme in solution (S#) and attached to the carbon nanotube (C#) are compared against the experimental (Exp) structures without the ligand (PDB:1QTV) (top: lysozyme) and with the peptidoglycan ligand (PDB:148L) (bottom: lysozyme-ligand). The root mean square deviation (RMSD) is computed on the backbone atoms (N, C α , C and O). The contact similarity indicates the percentage of the experimental residue–residue contacts that are preserved during the simulations. The mean and the standard deviation on the converged interval (see ESI) are shown for each simulation (S# and C#) and over all simulations (S-Avg and C-Avg)

Sim	RMSD (Å)	Secondary structure			Contact (%)
		α -Helix (%)	β -Sheet (%)	Coil (%)	
Lysozyme					
Exp	—	63.4	8.5	11.0	—
S-Avg	0.98 \pm 0.01	61.0 \pm 0.9	8.30 \pm 0.01	11.9 \pm 0.2	92.4 \pm 0.2
C-Avg	1.41 \pm 0.75	60.7 \pm 0.6	8.27 \pm 0.08	11.9 \pm 0.1	92.2 \pm 0.8
S1	1.00 \pm 0.30	60.1 \pm 1.3	8.3 \pm 1.2	12.1 \pm 1.0	92.2 \pm 0.9
S2	0.97 \pm 0.14	62.0 \pm 1.7	8.3 \pm 1.0	11.6 \pm 1.1	92.7 \pm 0.9
C1	1.19 \pm 0.50	61.2 \pm 1.9	8.3 \pm 1.1	11.9 \pm 1.1	91.5 \pm 1.2
C2	2.89 \pm 0.48	59.9 \pm 1.4	8.2 \pm 0.9	11.9 \pm 1.0	91.1 \pm 0.8
C3	0.93 \pm 0.14	61.4 \pm 1.8	8.3 \pm 1.0	11.7 \pm 1.1	93.0 \pm 0.9
C4	1.01 \pm 0.24	60.8 \pm 2.0	8.4 \pm 1.0	11.8 \pm 1.1	93.0 \pm 1.0
C5	1.01 \pm 0.19	60.4 \pm 1.4	8.2 \pm 0.8	12.1 \pm 1.0	92.5 \pm 0.9
Lysozyme–ligand					
Exp	—	62.2	8.5	11.6	—
S-Avg	1.43 \pm 0.01	61.8 \pm 0.1	8.52 \pm 0.04	11.7 \pm 0.1	92.9 \pm 0.3
C-Avg	1.88 \pm 0.33	61.0 \pm 0.1	8.02 \pm 0.60	11.9 \pm 0.3	91.9 \pm 0.4
S1	1.48 \pm 0.21	61.8 \pm 1.8	8.5 \pm 1.6	11.8 \pm 1.4	92.6 \pm 1.1
S2	1.38 \pm 0.17	61.7 \pm 1.8	8.6 \pm 1.5	11.6 \pm 1.3	93.2 \pm 0.8
C1	2.79 \pm 0.54	61.1 \pm 2.1	8.1 \pm 1.2	11.7 \pm 1.2	91.1 \pm 0.9
C2	2.10 \pm 0.29	61.0 \pm 1.7	7.7 \pm 1.3	12.2 \pm 1.2	92.0 \pm 0.9
C3	1.43 \pm 0.15	60.7 \pm 1.7	8.7 \pm 1.5	12.1 \pm 1.3	92.2 \pm 0.8
C4	2.00 \pm 0.31	61.1 \pm 1.8	7.1 \pm 1.4	11.7 \pm 1.2	92.0 \pm 0.9
C5	1.49 \pm 0.18	60.9 \pm 1.8	8.5 \pm 1.6	11.6 \pm 1.3	92.3 \pm 0.9

that the nanotube increases the RMSD as calculated from the crystalline structure by only 0.40–0.45 Å, leaving the secondary and the intramolecular contacts of both systems intact (Table 1).

DNA. While there are no experimental structures to compare with, it is possible to assess the effect of the nanotube on the DNA systems by looking at the structural differences between the systems in solution and in the presence of the nanotube in terms of the number of residue–residue contacts, the number of base–base H-bonds and the radius of gyration (Table 2).

In solution, the ssDNA, initially extended, folds into compact hairpin structures characterized by a low radius of gyration and stabilized by residue–residue contacts as well as base–base H-bonds (S-Avg in the top part of Table 2). There are some structural differences between our two simulations (S1 and S2) in terms of global folds as shown by the difference in residue–residue contacts. For their part, the two simulations of the dsDNA structure undergo small variations over time in terms of residue–residue contacts and base–base H-bonds: the fold remains of type-B as initially (S1, S2 and S-Avg in the bottom part of Table 2).

When attached to a nanotube, the structural ensemble of the dsDNA is weakly affected: the number of residue–residue contacts and base–base H-bonds as well as the radius of gyration are the same in solution and in the presence of the nanotube (S-Avg and C-Avg in the bottom part of Table 2). The situation is very different for the ssDNA system as it samples a completely different structural ensemble when linked to a nanotube. More specifically, it forms extended structures on the surface of the nanotube as shown by the larger radius of

Table 2 Structural stability of the DNA systems. The MD trajectories in solution (S#) are compared to those obtained in the presence of the carbon nanotube (C#) for the single-stranded DNA (top: ssDNA) and the double-stranded DNA (bottom: dsDNA). The total number of contacts is calculated considering all nucleic acid pairs. The number of H-bonds is calculated for base–base interactions only. The radius of gyration R_g measures the compactness of the structures. The mean and the standard deviation on the converged interval (see ESI) are shown for each simulation (S# and C#) and over all simulations (S-Avg and C-Avg)

Sim	Contacts (nb)	H-Bonds (nb)	R_g (nm)
ssDNA			
S-Avg	15.5 \pm 2.4	5.3 \pm 0.3	0.83 \pm 0.01
C-Avg	6.3 \pm 1.6	1.7 \pm 0.1	1.17 \pm 0.03
S1	17.9 \pm 2.9	5.6 \pm 1.3	0.83 \pm 0.01
S2	13.2 \pm 2.2	5.0 \pm 1.4	0.84 \pm 0.01
C1	9.0 \pm 2.5	2.7 \pm 1.2	1.13 \pm 0.06
C2	6.7 \pm 3.3	1.8 \pm 1.1	1.19 \pm 0.04
C3	5.9 \pm 3.1	1.2 \pm 0.8	1.17 \pm 0.06
C4	4.0 \pm 2.4	1.6 \pm 1.0	1.22 \pm 0.09
C5	6.1 \pm 3.0	1.3 \pm 0.7	1.17 \pm 0.07
dsDNA			
S-Avg	40.9 \pm 0.2	23.7 \pm 0.3	1.186 \pm 0.003
C-Avg	41.4 \pm 0.2	23.8 \pm 0.1	1.181 \pm 0.001
S1	40.7 \pm 3.1	23.4 \pm 1.5	1.19 \pm 0.02
S2	41.0 \pm 3.1	24.0 \pm 1.5	1.18 \pm 0.02
C1	41.5 \pm 3.1	24.0 \pm 1.5	1.18 \pm 0.02
C2	41.8 \pm 3.4	23.7 \pm 1.5	1.18 \pm 0.02
C3	41.2 \pm 3.1	23.7 \pm 1.5	1.18 \pm 0.02
C4	41.4 \pm 3.1	24.0 \pm 1.5	1.18 \pm 0.02
C5	41.2 \pm 3.1	23.8 \pm 1.5	1.18 \pm 0.02

gyration as well as by the reduced number of intramolecular contacts and H-bonds (S-Avg and C-Avg in the top part of Table 2).

Overall, the nanotube does not impact significantly the fold of biomolecules that are stabilized by several interactions such as the lysozyme and the double-stranded type-B DNA. However, the structural ensemble of the single-stranded DNA is significantly perturbed because it forms many contacts with the nanotube, as described in the next section.

Interactions with the nanotube

We now turn our attention on two classes of interactions that are thought to influence the electrical response of the carbon nanotube: (1) direct contacts and (2) charged groups within the Debye length of the anchor point between the biomolecule and the nanotube.^{19,22,78} Interactions with the nanotube are described in terms of the average minimal distance between each residue of the biomolecules and the carbon nanotube (Fig. 2).

Lysozyme. For the lysozyme, the helix-turn-helix motif between amino acids 115 and 134, which is spatially localized near S90C where the anchor is attached, is nearest to the nanotube (Fig. 2A and B). In the absence of the ligand, Gln-123 (*n*) and Arg-125 (+) are in direct contact with the nanotube, while other charged residues are found within 1 nm – approximate Debye length in a 100 mM NaCl solution at room temperature – of the nanotube: Arg-119 (+), Lys-124 (+), Asp-127 (–) and Glu-128 (–). In the presence of the ligand, the position of each residue from the nanotube shows a similar global trend compared to when the ligand is absent. More specifically, the same direct contacts and charged residues are found within 1 nm of the nanotube. For both states of the lysozyme, the net charge near the nanotube is globally positive.

Simulation C4 of the lysozyme without the ligand samples a different interaction pattern with the carbon nanotube (Fig. S11, ESI†). More specifically, residues Arg-95 (+), Lys-124 (+), Trp-126 (*n*), Asp-127 (–), Arg-157 (+) and Thr-155 (*n*) are now in contact with the nanotube along with Gln-123 (*n*) and

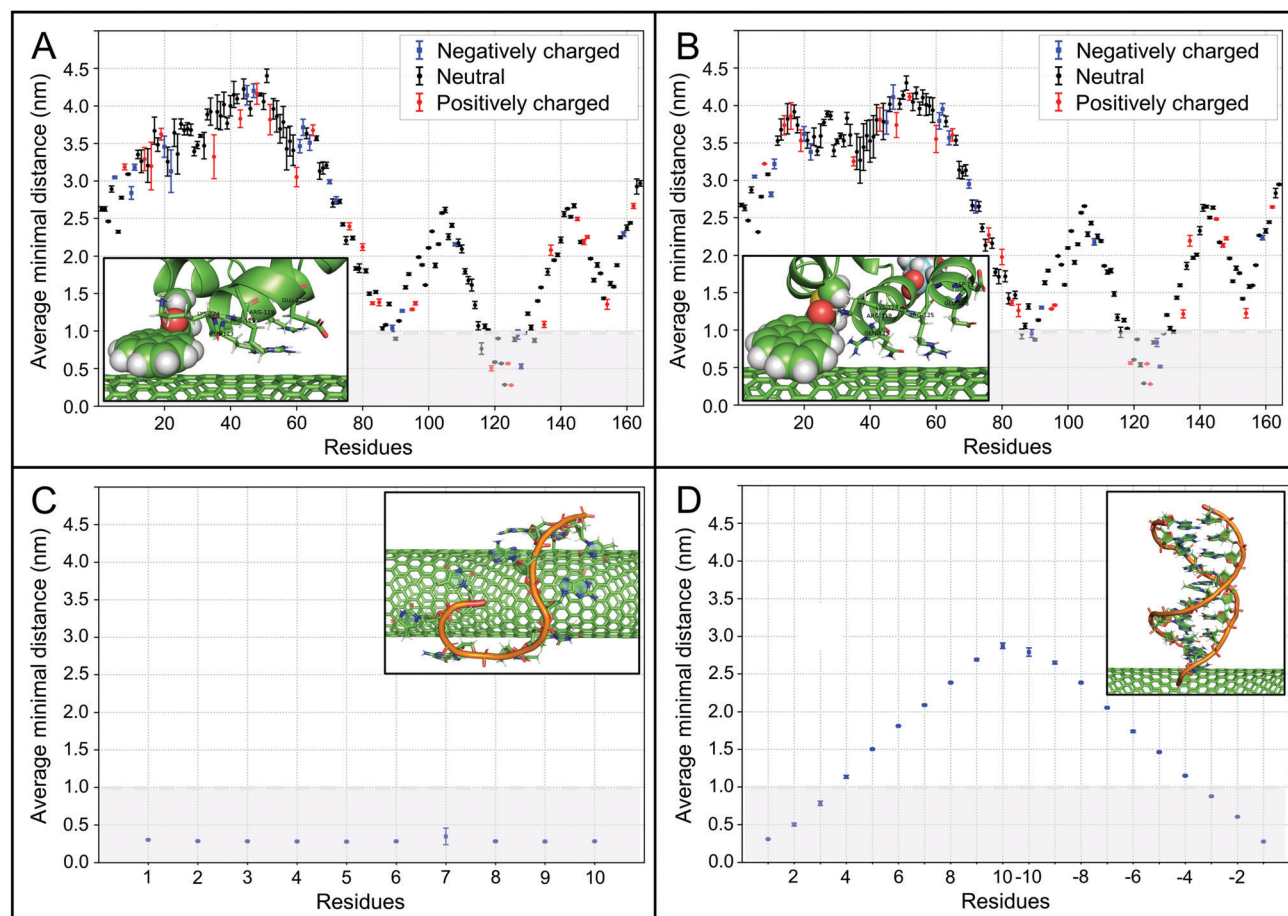


Fig. 2 Interactions with the carbon nanotube. The average minimal distance between the carbon nanotube and (A and B) the amino acids of the lysozyme or (C and D) the nucleic acids of the DNA sequence. Lysozyme (A) without the ligand and (B) with the peptidoglycan ligand. The lysozyme is attached to the nanotube by a pyrene-maleimide anchor covalently linked to S90C. The 5'-GTGAGTTGTT-3' DNA sequence (C) single-stranded and (D) type-B double-stranded. A single DNA strand is covalently attached to the carbon nanotube by an amide group at its 5'-end. The error bars correspond to a 1 – σ standard deviation. Statistics are computed from the average values of the five independent simulations on the converged interval for each system; except simulation C4 for the lysozyme without the ligand and simulation C1 for the single-stranded DNA, which are presented in the Supplementary Information. The grey region from 0 to 1 nm represents the Debye length in a 100 mM monovalent water solution at room temperature.

Arg-125 (+). The global orientation of the lysozyme with respect to the nanotube is also different: the lysozyme is localized more on the side of the nanotube. Nonetheless, the net charge near the nanotube remains globally positive.

DNA. For the DNA systems, the number of direct contacts and the positions of the nucleic acids from the nanotube are very different for ssDNA and dsDNA (Fig. 2C and D). For ssDNA, several aromatic contacts are observed with the nanotube causing, as seen previously, the DNA strand to sample more extended structures such that all its residues are in contact with the nanotube. In contrast, for the double-stranded state, only two contacts are observed with the nanotube. These two contacts are localized near the graft point: residue 1 at the 5'-end of the strand covalently attached to the nanotube and residue 20 at the 3'-end of the second strand. Consequently, the principal axis of the double-stranded structure relatively stays in a upward orientation with respect to the nanotube as seen by the position of the two other termini localized at around 2.5–3.0 nm from the nanotube. Finally, in contrast to the lysozyme, the DNA sequence is highly charged: the phosphate group of each nucleic acid possesses a net charge of $-1e$. The number of charged residues near the nanotube is therefore greater: all ten residues of ssDNA are within 1 nm of the nanotube, while only six residues are within this distance of the nanotube for dsDNA.

Simulation C1 of ssDNA samples a different interaction pattern with the carbon nanotube (Fig. S12, ESI[†]). Its configurations have fewer contacts with the nanotube because residues 5 to 8 are stacked. Nonetheless, the DNA strand remains near the carbon, with all residues being within 1.0 nm of it.

Overall, we observe few direct contacts between these systems and the nanotube, except for ssDNA. Also, we note the presence of several charged residues within 1.0 nm from the nanotube; these are largely responsible for the electrostatic potential variation on the surface of the nanotube, as presented next.

Electrostatic potential on the nanotube

The electrostatic potential generated by the biomolecules on the surface of the carbon nanotube is thought to cause the current variation experimentally measured in the bioFET.^{19,22} To assess this effect, we quantify the electrostatic potential as a function of the state of the biomolecules and as a function of the salt concentration.

The average electrostatic potential (ESP) on the nanotube is shown in Fig. 3 for each system. For both lysozyme systems, the ESP is positive and is localized near the anchor with the nanotube, as expected from the contact analysis in Fig. 2A and B. More precisely, the greatest ESP values are found within 2 nm of the anchor point along the nanotube and are spread over a region of $\sim 100^\circ$ around the nanotube, or slightly more than a quarter of the circumference. For both DNA systems, the ESP is negative and is mainly localized near the graft point. However, the ESP distribution generated by the ssDNA covers a larger surface compared with that of dsDNA with a spread around the nanotube extending over $\sim 200^\circ$ versus $\sim 50^\circ$, respectively. This is expected from the contact analysis showing that ssDNA spreads around the nanotube and forms many contacts with it (Fig. 2C and D).

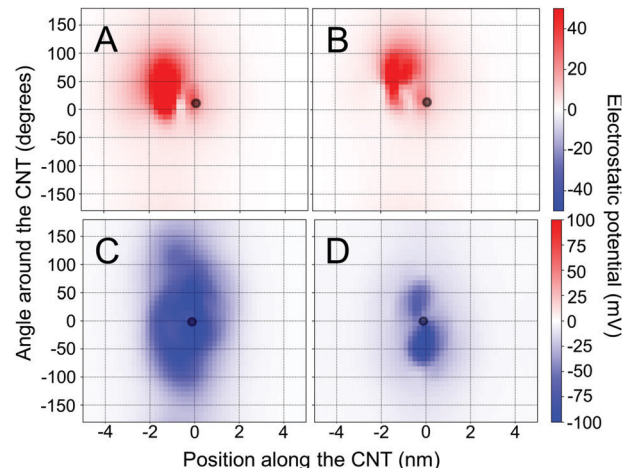


Fig. 3 Average electrostatic potential on the carbon nanotube. The average electrostatic potential (ESP) generated by the lysozyme – (A) without ligand and (B) with ligand – and by the DNA – (C) single-stranded and (D) double-stranded – is shown as a function of the position along the principal axis of the nanotube and the angle around the nanotube. The average is calculated on the independent simulations using the converged interval for each (see ESI[†]); except simulation C4 for the lysozyme without the ligand and simulation C1 for the single-stranded DNA, which are presented in the Supplementary Information. The black circle indicates (A and B) the center-of-mass position of the anchor's pyrene atoms and (C and D) the nanotube carbon atom that is covalently grafted to the DNA strand.

The overall electrostatic potential (ESP) time-averaged distributions on the nanotube are shown in Fig. 4. The ESP fluctuations for all four systems can be described by Gaussian distributions. For the lysozyme, the overall ESP is more positive in the absence of the bound ligand: $(22.9 \pm 6.2) \times 10^3$ (without ligand) and $(15.0 \pm 5.1) \times 10^3$ (with ligand). For the DNA systems, the global ESP is more negative for ssDNA: $(-78.5 \pm 9.9) \times 10^3$ (single-stranded) vs. $(-37.9 \pm 4.6) \times 10^3$ (double-stranded). For all systems, the ESP fluctuations over time are similar as those suggested by the standard deviation of the Gaussian distributions. However, while there is an overlap between the distributions of the two states of the lysozyme, those of the DNA states are well separated. This is coherent with the biomolecule–nanotube interactions as both lysozyme states have similar residues–nanotube distance distributions, while they are very different for both DNA states (Fig. 2). Looking more precisely at the lysozyme–ligand system, the peptidoglycan ligand, with its carboxylate groups, is shown to contribute to the overall ESP difference between the two systems (Fig. S19, ESI[†]). Indeed removing the ligand and keeping the same structure for the lysozyme shifts, for simulation C3, the overall ESP to more positive values from $(15.4 \pm 5.2) \times 10^3$ to $(19.2 \pm 5.4) \times 10^3$, which is less distant from the distribution $-(22.9 \pm 6.2) \times 10^3$ – for the lysozyme system.

The effect of the ion concentration on the overall electrostatic potential (ESP) on the nanotube is shown in Fig. 5. As expected, the ESP generated by the biomolecules on the surface of the nanotube decreases with increasing ion concentration because of the electrostatic screening provided by

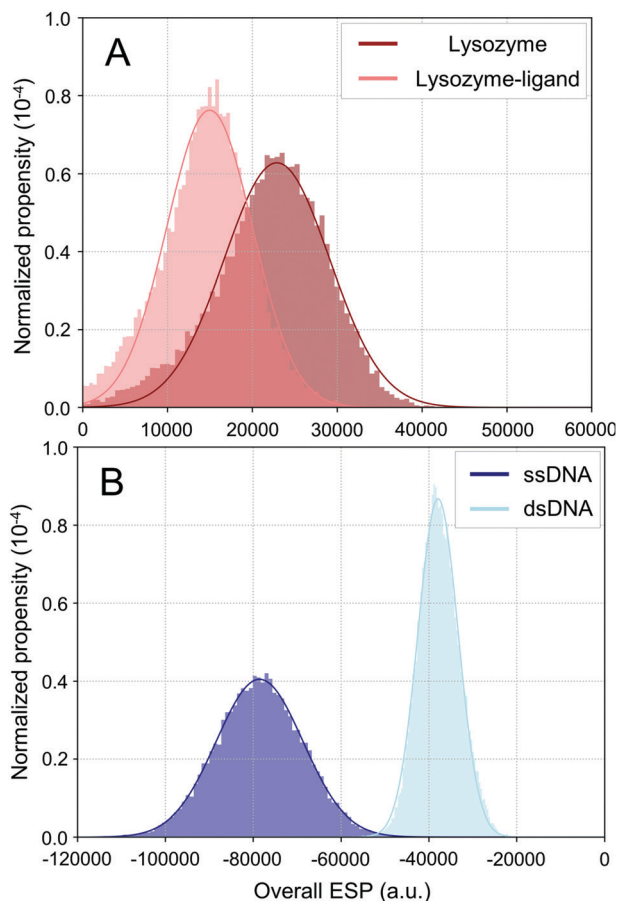


Fig. 4 Global electrostatic potential on the nanotube. The Riemann sum of the electrostatic potential over the surface of the nanotube is computed for each configuration in the converged interval of the MD trajectories, then the histogram is computed over the values obtained for all these configurations; except simulation C4 for the lysozyme without the ligand and simulation C1 for the single-stranded DNA, which are presented in the Supplementary Information. A Gaussian fit is performed on the histograms to extract their average and standard deviation. (A) The lysozyme without the ligand in dark red is compared to with the ligand in pale red. (B) Single-stranded DNA in dark blue is compared to double-stranded DNA in pale blue.

electrolytes in the solution. However, the magnitude of this effect is not the same depending on the state of the biomolecules. More precisely, the difference between the ESP generated by the lysozyme, with and without the ligand, is reduced as the concentration increases, while it is the opposite for the two DNA systems. Indeed, it is expected that the ESP generated by ssDNA will be less screened because it is globally nearer to the nanotube when compared to dsDNA (Fig. 2C and D). The origin of this asymmetry is however less obvious for the lysozyme for which only small differences are observed between the two systems as to the position of the charged residues with respect to the nanotube (Fig. 2A and B).

Overall, the electrostatic potential (ESP) generated by the biomolecules on the nanotube depends significantly on their state. The global ESP distributions of the lysozyme and the DNA systems have different characteristics, which can be related to

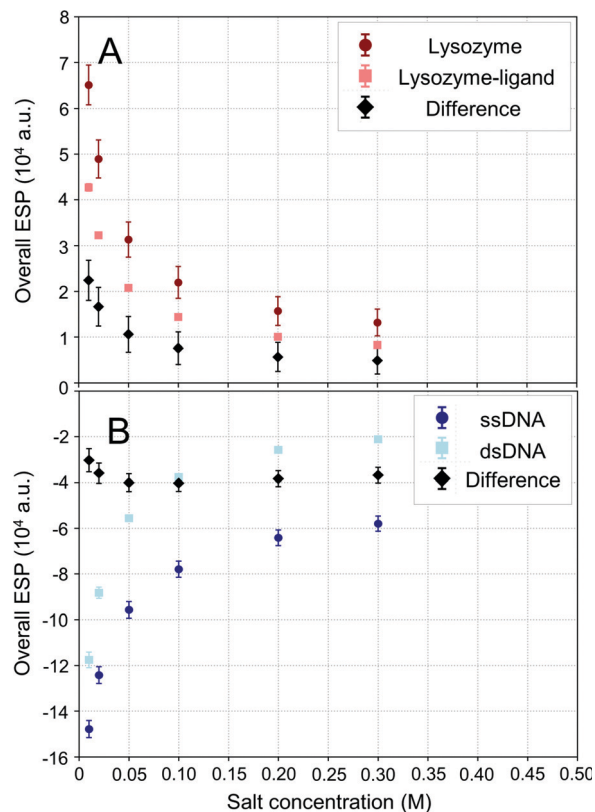


Fig. 5 Ionic salt concentration effect. The Riemann sum of the electrostatic potential (ESP) over the surface of the nanotube is computed for each configuration in the converged interval of the MD trajectories, then the average and the standard deviation are calculated over the values obtained for all these configurations in the independent simulations; except simulation C4 for the lysozyme without the ligand and simulation C1 for the single-stranded DNA, which are presented in the ESI.† The ESP is computed for six different NaCl salt concentrations. The error bars correspond to a $1 - \sigma$ standard deviation. (A) The lysozyme without the ligand in circle dark red is compared to with the ligand in square pale red. (B) The single-stranded DNA in circle dark blue is compared to the double-stranded DNA in square pale blue. The difference between the two states is shown in black.

current variation measured experimentally by the biosensor, as presented next.

Discussion

In this study, we investigate the molecular origin of the electrostatic gating of a carbon nanotube biosensor for two systems previously characterized experimentally using this device: the function of the lysozyme^{14,22} and the hybridization of DNA strands.^{15,19} We now further elaborate on our three main objectives: (1) evaluate the effect of the nanotube on the structural stability of the biomolecules, (2) describe the main interactions between the biomolecules and the nanotube and (3) characterize the electrostatic potential generated by the biomolecules on the surface of the nanotube.

Towards the first objective, we determine that the structural ensembles of both lysozyme systems and the double-stranded

DNA are not significantly affected by the nanotube, while that of the single-stranded DNA is (Tables 1 and 2). This is coherent with the experimental characterization of the carbon nanotube biosensor showing that the nanotube does not impact significantly the kinetic rates measured for these two systems when compared to the values obtained by other techniques such as single-molecule FRET.^{14,15,19,22}

That being said, the analysis of Sorgenfrei *et al.* also revealed that the kinetics of DNA hybridization measured by their carbon nanotube bioFET is best described by two double exponential fits, associated to two distinct processes.¹⁵ They argued that one process is associated with the hybridization taking place on the surface of the nanotube, while the other is associated with the hybridization taking place when the DNA strand is mostly extended in the solution. Moreover, they observed extended periods of time during which no hybridization is taking place, which they rationalized by the presence of inactivated states due to specific DNA–nanotube interactions. While the sampling of our simulations is not enough to characterize entirely the kinetics of DNA–nanotube interactions, our model highlights configurations in which the single-stranded DNA system indeed extends itself on the surface of the nanotube and interacts strongly with it throughout the simulations (Fig. 2C). We expect that the DNA has to progressively dissociate itself from the nanotube during dimerization to adopt a relatively upward orientation with respect to the nanotube as seen for the double-stranded DNA system (Fig. 2D).

Our result on single-stranded DNA (ssDNA)–nanotube interactions are in line with previous MD simulations.^{51–56} More precisely, ssDNA samples a variety of structures – extended, loop and partial wrapping, but not complete wrapping nor ring – stabilized by aromatic interactions with the nanotube and by intramolecular H-bonds and contacts (Table 2). As in these previous simulations, ssDNA binds quickly on the surface of the nanotube and does not detach from it. It therefore seems that the covalent tethering of the DNA strand to the nanotube does not impact much its structural ensemble. While there are many studies looking at the interactions of single-stranded DNA with carbon nanotubes, the interactions between double-stranded DNA and the nanotube are not something that has been much investigated, to our knowledge, using MD simulations. Our results indicate that the nanotube does not destabilize significantly double-stranded DNA motifs, in line with another MD simulation,⁵⁰ even when they are covalently tethered by one of their terminations.

With respect to the second objective, we monitored the direct contacts between biomolecules and the nanotube as these are expected to affect most strongly the conductance of the nanotube. We observe that few direct contacts with the nanotube are seen for both states of the lysozyme and for the double-stranded DNA, while the single-stranded DNA has many contacts (Fig. 2). More precisely, the nanotube interacts with aliphatic carbons of the lysozyme, while it interacts with the aromatic groups of the nucleic bases of the DNA systems. Interestingly, *ab initio* calculations shows that single-nucleotide

or amino acid contacts with the carbon nanotube are sufficient to impact its electronic structure, even though charge transfer with the nanotube is very small.^{38,40,42} In the case of nucleotides, the negatively charged phosphate group has a central role in this effect by locally polarizing the nanotube.

Finally, we show that the electrostatic potential (ESP) differs significantly between the lysozyme without and with the ligand and between the single- and double-stranded DNA (Fig. 3–5). These results can be related to the conductance fluctuations measured by the carbon nanotube biosensor for lysozyme function²² and for the hybridization of the 5'-GTGAGTTGTT-3' DNA sequence.¹⁹

For lysozyme, Choi *et al.* observed that the conductance as a function of time is described by a two-state distribution whose transition kinetic correlates with the catalytic activity of the lysozyme enzyme, with the high-conductance state corresponding to the ligand bound state.²² These two distributions partially overlap even if their average is different (see their Fig. 4) suggesting that the two states of the lysozyme should share similar interaction features with the nanotube. In line with experiment, our simulations find that the lysozyme–nanotube contacts are the same for the two states (Fig. 2) and that the ESP distributions partially overlap even if their average is different (Fig. 4). Furthermore, the effect of the positive ESP generated near the anchor point by both lysozyme conformations (Fig. 3) can be represented electronically as an effective decrease in the local density of charge carriers, since charge carriers are positive in the nanotube system used experimentally.^{14,22} Also, since the ligand bound state generates a less positive ESP, the local distortion of the conductance bands at the anchor site should be less pronounced, which is compatible with less scattering and hence a higher conductance level, as observed in the experiments.^{14,22} The precise coupling mechanisms and quantitative relationship between the highly localized ESP and charge transport along the nanotube remain to be explored at the *ab initio* level.

Choi *et al.* further showed that the magnitude of the conductance fluctuations between the two systems decreases as the buffer salt concentration increases (see their Fig. 2).²² Our simulations confirm that small structural differences between the two states of the lysozyme are sufficient for the ESP generated by the two states to be differently affected by the salt concentration (see Fig. 2 and 5). As a result the overall ESP gets more similar for the two systems as the salt concentration increases, in line with the reduced amplitude in the conductance fluctuations observed experimentally.

Finally, Choi *et al.* looked at K83 and R119 mutations, which they deemed important when looking at their position in the crystal structures of the two states of the lysozyme with respect to the S90C anchor point. They observed that changing their charge modifies the effective gating voltage suggesting that these residues are near the carbon nanotube (see their Fig. 4 and 5).²² Our simulations show that Arg-119 (+) is indeed near the nanotube in both states (0.50 ± 0.03 nm without and 0.56 ± 0.02 nm with the ligand) and contributes importantly to the ESP on the surface of the nanotube, while Lys-83 (+) is

farther (1.37 ± 0.02 nm without and 1.36 ± 0.03 nm with the ligand). Moreover, we observe that other charged residues are within 1.5 nm of the nanotube and are also contributing most to the ESP: Lys-85 (+), Asp-89 (−), Asp-92 (−), Arg-95 (+), Arg-96 (+), Lys-124 (+), Arg-125 (+), Asp-127 (−), Glu-128 (−), Lys-135 (+) and Arg-154 (+). The total charge of these residues is $+5e$.

When comparing their change in position between the two states, these residues should affect the magnitude of the conductance fluctuations differently. We choose to order those residues in decreasing order of their relative change of position between the two states calculated from $\Delta d/d \times 100\%$, where Δd is the position difference between the residue in the lysozyme vs in the lysozyme–ligand and d is the position of the residue in the ligand. This yields: Lys-135 (+11.7%), Arg-119 (+11.2%), Asp-92 (+2.6%), Arg-95 (−0.4%), Lys-83 (−0.5%), Arg-125 (−0.8%), Arg-96 (−2.7%), Lys-124 (−3.2%), Glu-128 (−3.2%), Asp-89 (−7.9%), Lys-85 (−8.8%), Arg-154 (−9.8%) and Asp-127 (−12.5%), with the positive (negative) values meaning that the residue in the lysozyme–ligand is nearer (farther) from the nanotube than the same residue in the lysozyme. While this suggests that Lys-83 would have a smaller effect than other charged residues, Arg-119 would have the strongest effect on the variation of the electrostatic potential if one only look at the distances involved. We also expect other residues to contribute to some extent to the overall ESP because the minimal distance of each residue to the nanotube (or to the anchor site) can pass through the protein, which is a region with an overall lower dielectric value with no electrostatic screening due to free ions, as we saw for the ligand for instance (Fig. S19, ESI[†]).

For the 5′-GTGAGTTGTT-3′ DNA sequence, Sorgenfrei *et al.* observed that the conductance as a function of time can be described by a two-state distribution whose transition kinetics correlates with the hybridization of small DNA fragments.¹⁹ These two distributions do not significantly overlap (see their Fig. 2), contrary to the lysozyme. Our simulations show a similar behaviour: the overall ESP distributions of the two DNA states do not overlap, contrary to the lysozyme (Fig. 4). This is consequent from the fact that DNA strands bear significant charge on the phosphate backbone, and that the simulated conformations for the single- and double-stranded DNA differ drastically, in particular in terms of the proximity of nucleotides to the nanotube surface: it is therefore coherent to have a large difference between the ESP profiles. However, in the experimental data, the single-stranded DNA is clearly associated with the high-conductance state based on thermodynamic and kinetic analysis of both states. In our simulations, the single-stranded DNA generates a more negative ESP than the double-stranded DNA on the surface of the nanotube, which would be expected to translate in a stronger distortion of the local electronic structure and thus a lower conductance due to scattering effects. It should however be noted that the DNA is tethered to a covalent defect in the nanotube, which is not the case for the lysozyme, and that such defects are known to generate localized electronic states that already have a complex interplay with the nanotube conductance.⁷⁹ It is however not clear how the negative ESPs due to the single- and

double-stranded DNA compound with such electronic states at the covalent defect site; such an analysis would require *ab initio* simulations of the electronic structure and charge transport.

It should be noted that the localized gating mechanisms just described for single-point functionalization cannot necessarily be transposed to when the nanotube is functionalized over most of its surface. Indeed, two experimental studies using such functionalization – with coverage by streptavidin proteins⁸⁰ or wrapping by DNA strands⁹ over the majority of the nanotube's surface – observed that DNA hybridization leads to an increase in the current, as opposed to what Sorgenfrei *et al.* measured when using single-point functionalization. These cases present two major differences with our study: (1) the DNA strands cannot directly interact with the nanotube due to the large linkers, and (2) the change of ESP during DNA hybridization should affect the global charge carrier density. Specifically, DNA hybridization should increase the overall magnitude of the negative ESP on the surface of the nanotube, thus increasing the current by globally increasing the density of positive charge carriers, in a manner similar to the gate electrode. The length-scale of the transition between the localized picture of electrostatic gating in these devices – dominated by scattering and local states – and the delocalized picture – dominated by the global carrier density – remains yet to be explored.

Returning to Sorgenfrei *et al.*, they also observed that the magnitude of the conductance fluctuations between the two states decreases as the buffer salt concentration increases (see their Fig. 4), like in the case of the lysozyme.¹⁹ However, our calculations based on the simulated ESP profiles predicts the opposite trend: because the single-stranded DNA is globally localized closer to the nanotube surface, it generates the larger ESP and is also less effectively screened when increasing ionic concentration, compared to the double-stranded DNA. The difference between the two states should thus increase as the ionic concentration increases (Fig. 5). Furthermore, Sorgenfrei *et al.* also observed that removing the bases in the complementary DNA strand that are nearest from the nanotube reduces the amplitude of conductance fluctuations (see their Fig. 3).¹⁹ However, from our results, we would expect the opposite because the overall ESP of the double-stranded DNA would then become less negative, thus increasing the ESP gap between the two states (see Fig. 4).

The unforeseen trends observed with the conductance states, *i.e.* their response to salt concentration, base suppression, and even possibly their respective high/low conductance order, raise interesting questions, especially since our simulated conformations for the DNA, as discussed earlier, appear consistent with reported interactions between single- and double-stranded DNA and carbon nanotubes in solution, both in theoretical and experimental studies. Differences between the experiments and the simulations include the contribution of non-specific adsorption of DNA strands along the nanotube; however, this should affect the global conductance, as observed by Sorgenfrei *et al.* when non-specific binding of single-stranded DNA occurs on the nanotube over time, but should

have little effect on the conductance fluctuations.¹⁹ Rather, we expect that the discrepancies could arise from the influence of parameters that are specific to the bioFET configuration, such as the nanotube doping state and/or the surrounding applied potentials. DNA structures could be particularly susceptible to such features because they are highly charged, contrary to most proteins such as the lysozyme, which would also explain the excellent agreement obtained for the latter.

Conclusions

In this study, we characterized the electrostatic potential (ESP) generated by biomolecules on the surface of a carbon nanotube used in the context of single-molecule field-effect biosensors (bioFET). To do so, we performed molecular dynamics simulations on two biomolecules whose kinetics was previously investigated using a carbon-nanotube bioFET: (1) the function of the lysozyme enzyme as it cleaves a peptidoglycan and (2) the hybridization of a DNA strand.

Our work showed that the proximity of the biomolecule generates an ESP at the surface of the nanotube, mainly localized near the graft/anchor point of the biomolecule, which is expected to generate a local alteration of the electronic structure of the nanotube. Moreover, we showed that this ESP depends significantly on the conformational state of the biomolecule. For the lysozyme, the calculated ESP profiles explain the two conductance levels measured experimentally by the bioFET, as well as their dependence with salt concentration. For the DNA, however, the predictions for the conductance and its salt concentration dependence from our calculated ESP profiles present a mixture of agreement and differences from the experimental observations. This suggests that additional mechanisms are influential to the conformational dynamics of DNA tethered to a nanotube FET device, possibly due to the highly-charged character of this molecule.

In light of our results, we believe that two new questions arise concerning the inner working of this carbon nanotube biosensor, that could be addressed in further simulation studies. First, the non-trivial interplay between external potentials applied in the bioFET device (gate and source-drain), the ion distribution in the electrolyte and the biomolecule conformation should be carefully investigated. Second, the impact on the nanotube conductance from the electrostatic potential generated by large biomolecules on its the surface should be precisely characterized using QM/MM techniques, to better understand the combined effects originating from the local perturbation of electronic states by the anchoring defect and by the ESP from the biomolecule, as well as any resulting scattering effects. In that regards, the structural ensemble obtained for the lysozyme and the 10-nt DNA sequence in our study could be used as a starting point for such simulations.

Author contributions

S. C. roles: conceptualization, data curation, formal analysis, funding acquisition, investigation, methodology, resources,

software, supervision, validation, visualization, writing – original draft and writing – review and editing. D. B. roles: conceptualization, methodology, supervision, validation and writing – review and editing. N. M. roles: funding acquisition, resources, supervision, validation and writing – review and editing.

Conflicts of interest

There are no conflicts to declare.

Acknowledgements

Sébastien Côté acknowledges the support from the Fonds de recherche du Québec – Nature et technologie (FRQ-NT #275304), Delphine Bouilly the support from her Canada Research Chair Tier 2 in Bionanoelectronics and Normand Mousseau the support of the Natural Sciences and Engineering Research Council of Canada through a Discovery Grant. The authors also acknowledge Dylan Tassé and Sandrine St-Cyr for preliminary tests on the lysozyme system. This research was enabled in part by support provided by Calcul Québec (www.calculquebec.ca) and Compute Canada (www.computeCanada.ca).

References

- H. Li, W. Shi, J. Song, H.-J. Jang, J. Dailey, J. Yu and H. E. Katz, *Chem. Rev.*, 2019, **119**, 3–35.
- C. Anichini, W. Czepa, D. Pakulski, A. Aliprandi, A. Ciesielski and P. Samori, *Chem. Soc. Rev.*, 2018, **47**, 4860–4908.
- M. Kaisti, *Biosens. Bioelectron.*, 2017, **98**, 437–448.
- R. Ahmad, T. Mahmoudi, M.-S. Ahn and Y.-B. Hahn, *Biosens. Bioelectron.*, 2018, **100**, 312–325.
- A. Zhang and C. M. Lieber, *Chem. Rev.*, 2016, **116**, 215–257.
- B. L. Allen, P. D. Kichambare and A. Star, *Adv. Mater.*, 2007, **19**, 1439–1451.
- A. Beraud, M. Sauvage, C. M. Bazan, M. Tie, A. Bencherif and D. Bouilly, *Analyst*, 2021, **146**, 403–428.
- R. Rautela, S. Scarfe, J. M. Guay, P. Lazar, M. Pykal, S. Azimi, C. Grenapin, J. Boddison-Chouinard, A. Halpin, W. Wang, L. Andrzejewski, R. Plumadore, J. Park, J. M. Menard, M. Otyepka and A. Luican-Mayer, *ACS Appl. Mater. Interfaces*, 2020, **12**, 39764–39771.
- X. Xu, P. Clement, J. Eklof-Osterberg, N. Kelley-Loughnane, K. Moth-Poulsen, J. L. Chavez and M. Palma, *Nano Lett.*, 2018, **18**, 4130–4135.
- S. Li, K. Huang, Q. Fan, S. Yang, T. Shen, T. Mei, J. Wang, X. Wang, G. Chang and J. Li, *Biosens. Bioelectron.*, 2019, **136**, 91–96.
- K. Melzer, A. M. Munzer, E. Jaworska, K. Maksymiuk, A. Michalska and G. Scarpa, *Analyst*, 2014, **139**, 4947–4954.
- A. M. Munzer, W. Seo, G. J. Morgan, Z. P. Michael, Y. Zhao, K. Melzer, G. Scarpa and A. Star, *J. Phys. Chem. C*, 2014, **118**, 17193–17199.
- J. Wang, F. Shen, Z. Wang, G. He, J. Qin, N. Cheng, M. Yao, L. Li and X. Guo, *Angew. Chem., Int. Ed.*, 2014, **53**, 5038–5043.

- 14 Y. Choi, I. S. Moody, P. C. Sims, S. R. Hunt, B. L. Corso, I. Perez, G. A. Weiss and P. G. Collins, *Science*, 2012, **335**, 319–324.
- 15 S. Sorgenfrei, C.-y. Chiu, J. Gonzalez, Jr., Y.-J. Yu, P. Kim, C. Nuckolls and K. L. Shepard, *Nat. Nanotechnol.*, 2011, **6**, 126–132.
- 16 D. Bouilly, J. Hon, N. S. Daly, S. Trocchia, S. Vernick, J. Yu, S. Warren, Y. Wu, R. L. Gonzalez, Jr., K. L. Shepard and C. Nuckolls, *Nano Lett.*, 2016, **16**, 4679–4685.
- 17 A. Zhang, J.-H. Lee and C. M. Lieber, *Nano Today*, 2021, **38**, 101135.
- 18 C. Gu, C. Jia and X. Guo, *Small Methods*, 2017, **1**, 1700071.
- 19 S. Sorgenfrei, C. Y. Chiu, M. Johnston, C. Nuckolls and K. L. Shepard, *Nano Lett.*, 2011, **11**, 3739–3743.
- 20 S. Vernick, S. M. Trocchia, S. B. Warren, S. B. Young, D. Bouilly, R. L. Gonzalez, C. Nuckolls and K. L. Shepard, *Nat. Commun.*, 2017, **8**, 15450.
- 21 Y. Lee, S. M. Trocchia, S. B. Warren, E. F. Young, S. Vernick and K. L. Shepard, *ACS Nano*, 2018, **12**, 9922–9930.
- 22 Y. Choi, T. J. Olsen, P. C. Sims, I. S. Moody, B. L. Corso, M. N. Dang, G. A. Weiss and P. G. Collins, *Nano Lett.*, 2013, **13**, 625–631.
- 23 K. M. Pugliese, O. T. Gul, Y. Choi, T. J. Olsen, P. C. Sims, P. G. Collins and G. A. Weiss, *J. Am. Chem. Soc.*, 2015, **137**, 9587–9594.
- 24 P. C. Sims, I. S. Moody, Y. Choi, C. Dong, M. Iftikhar, B. L. Corso, O. T. Gul, P. G. Collins and G. A. Weiss, *J. Am. Chem. Soc.*, 2013, **135**, 7861–7868.
- 25 S. O. Woo, M. Oh, L. Alhalhooly, J. Farmakes, A. J. Rajapakse, Z. Yang, P. G. Collins and Y. Choi, *J. Phys. Chem. B*, 2021, **125**, 5750–5756.
- 26 H. Kase, R. Negishi, M. Arifuku, N. Kiyoyanagi and Y. Kobayashi, *J. Appl. Phys.*, 2018, **124**, 064502.
- 27 O. T. Gul, K. M. Pugliese, Y. Choi, P. C. Sims, D. Pan, A. J. Rajapakse, G. A. Weiss and P. G. Collins, *Biosensors*, 2016, **6**, 1–19.
- 28 X. Xu, B. J. Bowen, R. E. A. Gwyther, M. Freeley, B. Grigorenko, A. V. Nemukhin, J. Eklof-Osterberg, K. Moth-Poulsen, D. D. Jones and M. Palma, *Angew. Chem., Int. Ed.*, 2021, **60**, 20184–20189.
- 29 S. You, J. Froberg, J. Yu, M. Haldar, A. Sedigh, S. Mallik, D. K. Srivastava and Y. Choi, *Chem. Commun.*, 2017, **53**, 3307–3310.
- 30 M. V. Akhterov, Y. Choi, T. J. Olsen, P. C. Sims, M. Iftikhar, O. T. Gul, B. L. Corso, G. A. Weiss and P. G. Collins, *ACS Chem. Biol.*, 2015, **10**, 1495–1501.
- 31 Y. Choi, G. A. Weiss and P. G. Collins, *Phys. Chem. Chem. Phys.*, 2013, **15**, 14879–14895.
- 32 J. Li, G. He, U. Hiroshi, W. Liu, H. Noji, C. Qi and X. Guo, *ACS Nano*, 2017, **11**, 12789–12795.
- 33 D. Umadevi, S. Panigrahi and G. N. Sastry, *Acc. Chem. Res.*, 2014, **47**, 2574–2581.
- 34 M. Chehel Amirani and T. Tang, *J. Biomol. Struct. Dyn.*, 2015, **33**, 1567–1597.
- 35 Electronic transport upon adsorption of biomolecules on graphene, in *Handbook of graphene*, ed. B. Palys, Scrivener Publishing LLC, 2019.
- 36 A. Das, A. K. Sood, P. K. Maiti, M. Das, R. Varadarajan and C. N. R. Rao, *Chem. Phys. Lett.*, 2008, **453**, 266–273.
- 37 S. Meng, P. Maragakis, C. Paploukas and E. Kaxiras, *Nano Lett.*, 2007, **7**, 45–50.
- 38 M. Chehelamirani, M. C. da Silva and D. R. Salahub, *Phys. Chem. Chem. Phys.*, 2017, **19**, 7333–7342.
- 39 C. Rajesh, C. Majumder, H. Mizuseki and Y. Kawazoe, *J. Chem. Phys.*, 2009, **130**, 124911.
- 40 D. Xiao, W. Sun, H. Dai, Y. Zhang, X. Qin, L. Li, Z. Wei and X. Chen, *J. Phys. Chem. C*, 2014, **118**, 20694–20701.
- 41 M. Chehel Amirani and T. Tang, *Phys. Chem. Chem. Phys.*, 2015, **17**, 7564–7575.
- 42 M. Chehel Amirani and T. Tang, *Nanoscale*, 2015, **7**, 19586–19595.
- 43 K. Umemura, *Nanomaterials*, 2015, **5**, 321–350.
- 44 H. Sun, J. Ren and X. Qu, *Acc. Chem. Res.*, 2016, **49**, 461–470.
- 45 M. Zheng, A. Jagota, E. D. Semke, B. A. Diner, R. S. McLean, S. R. Lustig, R. E. Richardson and N. G. Tassi, *Nat. Mater.*, 2003, **2**, 338–342.
- 46 M. Zheng, A. Jagota, M. S. Strano, A. P. Santos, P. Barone, S. G. Chou, B. A. Diner, M. S. Dresselhaus, R. S. McLean, G. B. Onoa, G. G. Samsonidze, E. D. Semke, M. Usrey and D. J. Walls, *Science*, 2003, **302**, 1545–1548.
- 47 F. Albertorio, M. E. Hughes, J. A. Golovchenko and D. Branton, *Nanotechnology*, 2009, **20**, 395101.
- 48 X. Tu, S. Manohar, A. Jagota and M. Zheng, *Nature*, 2009, **460**, 250–253.
- 49 Z. Li, Y. Song, A. Li, W. Xu and W. Zhang, *Nanoscale*, 2018, **10**, 18586–18596.
- 50 X. Zhao and J. K. Johnson, *J. Am. Chem. Soc.*, 2007, **129**, 10438–10445.
- 51 R. R. Johnson, A. T. C. Johnson and M. L. Klein, *Nano Lett.*, 2008, **8**, 69–75.
- 52 R. R. Johnson, A. Kohlmeyer, A. T. C. Johnson and M. L. Klein, *Nano Lett.*, 2009, **9**, 537–541.
- 53 W. Martin, W. Zhu and G. Krilov, *J. Phys. Chem. B*, 2008, **112**, 16076–16089.
- 54 D. Roxbury, J. Mittal and A. Jagota, *Nano Lett.*, 2012, **12**, 1464–1469.
- 55 D. Roxbury, A. Jagota and J. Mittal, *J. Phys. Chem. B*, 2013, **117**, 132–140.
- 56 A. A. Alizadehmojarad, X. Zhou, A. G. Beyene, K. E. Chacon, Y. Sung, R. L. Pinals, M. P. Landry and L. Vukovi, *Adv. Mater. Interfaces*, 2020, **7**, 2000353.
- 57 Y. Yu, H. Sun, K. Gilmore, T. Hou, S. Wang and Y. Li, *ACS Appl. Mater. Interfaces*, 2017, **9**, 32452–32462.
- 58 M. Noordadi, F. Mehrnejad, R. H. Sajedi, M. Jafari and B. Ranjbar, *PLoS One*, 2018, **13**, e0198519.
- 59 Schrödinger LLC, *The PyMOL molecular graphics system*, <https://pymol.org>.
- 60 M. J. Abraham, T. Murtola, R. Schulz, S. Páll, J. C. Smith, B. Hess and E. Lindahl, *SoftwareX*, 2015, **1–2**, 19–25.
- 61 G. Bussi, D. Donadio and M. Parrinello, *J. Chem. Phys.*, 2007, **126**, 014101.
- 62 B. Hess, *J. Chem. Theory Comput.*, 2008, **4**, 116–122.

- 63 S. Miyamoto and P. A. Kollman, *J. Comput. Chem.*, 1992, **13**, 952–962.
- 64 U. Essmann, L. Perera, M. L. Berkowitz, T. Darden, H. Lee and L. G. Pedersen, *J. Chem. Phys.*, 1995, **103**, 8577–8593.
- 65 W. L. Jorgensen, J. Chandrasekhar and J. D. Madura, *J. Chem. Phys.*, 1983, **79**, 926–935.
- 66 I. S. Joung and T. E. Cheatham, *J. Phys. Chem. B*, 2008, **112**, 9020–9041.
- 67 L. H. Kuroki, R. Weaver and B. W. Matthews, *Proc. Natl. Acad. Sci. U. S. A.*, 1999, **96**, 8949–8954.
- 68 L. H. Kuroki, R. Weaver and B. W. Matthews, *Science*, 1993, **262**, 2030–2033.
- 69 J. A. Maier, C. Martinez, K. Kasavajhala, L. Wickstrom, K. E. Hauser and C. Simmerling, *J. Chem. Theory Comput.*, 2015, **11**, 3696–3713.
- 70 J. Wang, R. M. Wolf, J. W. Caldwell, P. A. Kollman and D. A. Case, *J. Comput. Chem.*, 2004, **25**, 1157–1174.
- 71 A. W. S. da Silva and W. F. Vranken, *BMC Res. Notes*, 2012, **5**, 367.
- 72 A. Jakalian, D. B. Jack and C. I. Bayly, *J. Comput. Chem.*, 2002, **23**, 1623–1641.
- 73 P. Cieplak, W. D. Cornell, C. I. Bayly and P. A. Kollman, *J. Comput. Chem.*, 1995, **16**, 1357–1377.
- 74 R. Galindo-Murillo, J. C. Robertson, M. Zgarbová, J. Šponer, M. Otyepka, P. Jurečka and T. E. Cheatham, III, *J. Chem. Theory Comput.*, 2016, **12**, 4114–4127.
- 75 W. G. Touw, C. Baakman, J. Black, T. A. H. te Beek, E. Krieger, R. P. Joosten and G. Vriend, *Nuc. Acids Res.*, 2015, **43**, D364–D368.
- 76 W. Kabsch and C. Sander, *Biopolymers*, 1983, **22**, 2577–2637.
- 77 N. A. Baker, D. Sept, S. Joseph, M. J. Holst and J. A. McCammon, *Proc. Natl. Acad. Sci. U. S. A.*, 2001, **98**, 10037–10041.
- 78 E. Stern, R. Wagner, F. J. Sigworth, R. Breaker, T. M. Fahmy and M. A. Reed, *Nano Lett.*, 2007, **7**, 3405–3409.
- 79 D. Bouilly, J. L. Janssen, J. Cabana, M. Côté and R. Martel, *ACS Nano*, 2015, **9**, 2626–2634.
- 80 M. T. Martínez, Y.-C. Tseng, M. González and J. Bokor, *J. Phys. Chem. C*, 2012, **116**, 22579–22586.